PHYSICAL REVIEW A **100**, 013418 (2019)

Near-threshold photodetachment microscopy in the presence of a transverse magnetic field

K. Titimbo,[1,*] X. J. Chen,[1,2] and M. L. Du[1,2]
[1]*Institute of Theoretical Physics, Chinese Academy of Sciences, Beijing 100190, People's Republic of China*
[2]*School of Physical Sciences, University of Chinese Academy of Sciences, No.19A Yuquan Road, Beijing 100049, People's Republic of China*

(Received 3 May 2019; published 26 July 2019)

Near-threshold photodetachment microscopy of mononegative ions is theoretically studied when a homogeneous transverse magnetic field **B** is superimposed to the static electric field **E**. The electron flux distribution is obtained using two different approaches: the quantum source theory with the energy-Green function evaluated by means of the stationary phase approximation and the closed-orbit theory. Here we describe the physical ideas while developing the theory in detail. Both theoretical methods yield consistent descriptions for all field intensities and angular momentum of the detached electrons we have investigated and also reproduce reported experimental results. From our calculations, we have found that the presence of the transverse magnetic field leads to a global displacement of the recorded electron flux distribution along the **E** × **B** direction. Furthermore, we found that the shape of the recorded interference pattern changes from circular to elliptical as the magnetic field increases. We have theoretically characterized and quantified those effects on the interference pattern due to the presence of the transverse magnetic field.

DOI: 10.1103/PhysRevA.100.013418

I. INTRODUCTION

For the study of the matter-waves interference phenomena in atomic physics the electron properties have been widely used [1–4]. Hence electron interference effects rapidly became the core of photodetachment microscopy experiments [5–7], that is a technique introduced to describe the process of observing and measuring the phenomenon of photoelectrons interference [8–10]. The crucial idea considers electrons, produced due to photodetachment of negative ions in the presence of a uniform static electric field, and the field accelerates the electron towards a position-sensitive two-dimensional detector located at a macroscopic distance, so that the photoelectron spatial distribution is observed from the signal recorded. Under this configuration the interference pattern observed shows concentric rings. This pattern is explained as the interference of the electrons following two classical paths linking the atom with the detector [11–13]. In this sense, the external field provides a virtual double-slit environment that allows for probing the energy of the emitted electron, and thereby the electron affinity of the ion, with extreme accuracy [14,15].

The relevance of the technique demanded the study of more complex field configurations. So far, the electron propagation in solely homogeneous magnetic field [16], as well as parallel electric and magnetic fields, has been studied theoretically [17,18]. In the aforementioned cases, the spatial electron distribution at the detector could be obtained in a closed form using quantum theory, but also by semiclassical methods that provide clear physical insights about the nature of the phenomenon. On the other hand, photodetachment microscopy in crossed electric and magnetic fields has been implemented experimentally [7], and some of their results have been discussed and explained from classical theory [19], but despite the attempts the theoretical quantum solution in a closed form is still absent [19–21]. From those experiments, it has been obtained that the combination of electric and magnetic fields imprints a nontrivial structure on the spatial electron distribution [18,22].

Recently, we have addressed the issue of the photodetachment microscopy in the presence of crossed homogeneous electric and magnetic field, from the theoretical point of view, using two approaches: the quantum source theory and the closed-orbit theory [22]. We obtained identical interference patterns out of the two theoretical approaches for given values of the angular momentum of the photoelectron. Our findings confirmed previous experimental [7] and theoretical [19] explanations: the presence of a perpendicular magnetic field produces a global displacement of the classical electron trajectories along the **E** × **B** direction, which is translated in a global displacement of the interference pattern in the recorded spatial electron distribution. Furthermore, we theoretically studied the effects of increasing the magnetic-field intensity into a region which has not been experimentally studied so far, unraveling that, in addition to the global displacement of the interference pattern, the shape of the pattern changes from circular to elliptical as the intensity of the field increases. We focused our attention on photoelectrons emitted with isotropic and anisotropic angular distribution, in particular, with angular momentum $l = 0, 1$, corresponding to s waves and p waves. In Fig. 1 a diagram showing the microscope configuration and effects of the magnetic field are depicted.

In this article, we aim to present the details of the theoretical formulation and the analytical expressions that allow one to fully quantify the effects of the perpendicular **B** field in near-threshold photodetachment microscopy of negative ions. Let us briefly describe the article structure. In Sec. II we present the physical situation under study and set the

---

[*] titimbo@itp.ac.cn

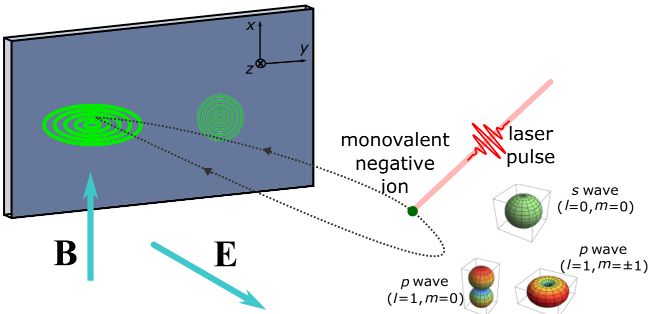

FIG. 1. Photodetachment microscopy from negative ions scheme. The electric and magnetic fields are perpendicular to each other. The emitted electron is considered not only isotropic (s waves) but also anisotropic (p waves). For p waves, sublevel $m = 0$ corresponds to a laser field polarized parallel to the electric field, whilst $m = -1, 1$ corresponds to perpendicular polarization. In the absence of magnetic field the spatial electron distribution shows concentric circular rings. Meanwhile, in the presence of the perpendicular magnetic field, the spatial distribution is displaced along the $\mathbf{E} \times \mathbf{B}$ direction and the interference rings are no longer circular.

magnitudes of the parameters for the numerical experiments. Section III is devoted to the study of the classical equation of motion describing the electron trajectories, as well as the caustic surface and the classically allowed region for the electrons arriving at the detection plane. In the following two sections we construct the outgoing electron wave function, for isotropic (s waves) and anisotropic (p waves) emissions. In detail, Sec. IV introduces the quantum source theory for the description of the wave function corresponding to the physical phenomena, while in Sec. V the closed-orbit theory is presented and the wave function constructed. Section VI describes the numerical results obtained from both theoretical approaches when the two-dimensional spatial distribution is recorded; the two main effects due to the presence of the transverse magnetic field are highlighted. Finally, in Sec. VII a discussion of the results and conclusions are presented.

II. PHOTODETACHMENT MICROSCOPY

In the photodetachment microscopy scheme electrons are detached from negatively charged ions X^- due to the interaction with a laser field: $X^- + \hbar\omega_l \rightarrow X + e^-$, where ω_l is the photon frequency of the laser. The electron is emitted with a definite energy $\mathcal{E} = \hbar\omega_l + \mathcal{E}_b$, with $\mathcal{E}_b$ the binding energy of the specific atomic species and with a given angular momentum. Here we focus our attention on the generation of electronic s waves and p waves [6,7,19,23–26]; for instance, these conditions have been achieved in experiments using S^- and H^-, respectively. Then, the electron wave propagates outward from the atomic source to a spatial region where external electric $\mathbf{E}$ and magnetic $\mathbf{B}$ fields are present. The configuration under study is such that the electric field accelerates the electron to a detection plate, while the magnetic field is oriented perpendicularly. Finally, the electron reaches a detector oriented perpendicular to the electric field and placed at macroscopic distances. The fields lead to the formation of an interference pattern on the detector. Favorable conditions for the conspicuous fringe occur when photoelectrons leave the atom mainly along the same direction as the electric field. This is achieved only for $m = 0$ in the case when photon polarization is parallel to the electric field, while for perpendicular polarization to the field $m = \pm 1$ [8].

Henceforth, for the theoretical model we will consider electrons with charge $-q$ (q the elementary charge) and mass m released outward from the monovalent anion with a definite energy $\mathcal{E}$ (near-threshold $\mathcal{E} \rightarrow 0$). The electric field is $\mathbf{E} = -E\,\hat{\mathbf{k}}$, $E > 0$, and transverse to it the magnetic field is $\mathbf{B} = B\,\hat{\mathbf{i}}$, $B > 0$. The detector is at $z = z_D$. A schematic view of the situation described is shown in Fig. 1. In order to numerically study the effects of the transverse magnetic field we are going to fix the following magnitudes: $E = 350$ V/m, $\mathcal{E} = 120\ \mu$eV, and the detector position $z_D = 0.50$ m, while varying the magnetic-field intensities.

Within the quantum theory, the physical system could be described by a total Hamiltonian of the form

$$\mathcal{H}_{\text{total}} = \frac{1}{2m}(\mathbf{p} + q\mathbf{A})^2 - q\Phi(\mathbf{r}) + \mathcal{V}_c + \mathcal{V}_L, \qquad (1)$$

where $\mathbf{p}$ is the momentum operator of the electron, $\mathbf{A}$ is the magnetic vector potential, and $\Phi(\mathbf{r})$ is the electric potential associated to the external fields. The potential $\mathcal{V}_c$ accounts for the interaction of the detached electron with the remaining atom and $\mathcal{V}_L$ takes into account the interaction with the laser pulse that produces the detachment.

In order to compare with experiments, the quantity of interest is the normal component to the detector of the current density distribution associated to the outgoing electron; it is given by

$$j_z(\mathbf{r}) = \frac{\hbar}{m}\mathrm{Im}[\psi(\mathbf{r})^*\,\nabla_z\psi(\mathbf{r})] + \frac{qA_z}{m}|\psi(\mathbf{r})|^2. \qquad (2)$$

This is directly related to the spatial distribution of photoelectrons recorded at the detector [20].

However, the solution of the corresponding Schrödinger equation for the photodetached electron wave function $\psi(\mathbf{r})$ is not available in a closed analytic form. Therefore, we consider that, sufficiently far from the atom, the wave propagates according to semiclassical mechanics and it is correlated to classical trajectories [20,21,27–29].

III. CLASSICAL MOTION

It is known that some properties of the classical motion prevail in the quantum-mechanical case. Given the robustness of semiclassical methods and in preparation for our later derivation of the electron wave function, we first develop the classical formalism describing the motion of the electron in external fields. Since in photodetachment from monovalent negative ions the remaining atom is neutral, we neglect the interaction with the remaining atom, i.e., Coulomb interaction. Similarly, for the sake of simplicity, we do not study the mechanism of generation of electrons. Therefore, we consider that the motion of the photoelectron is governed only by the force exerted by the external electric $\mathbf{E}$ and magnetic $\mathbf{B}$ fields. Standard Newtonian mechanics can be used to examine the classical trajectories that the photodetached electrons follow

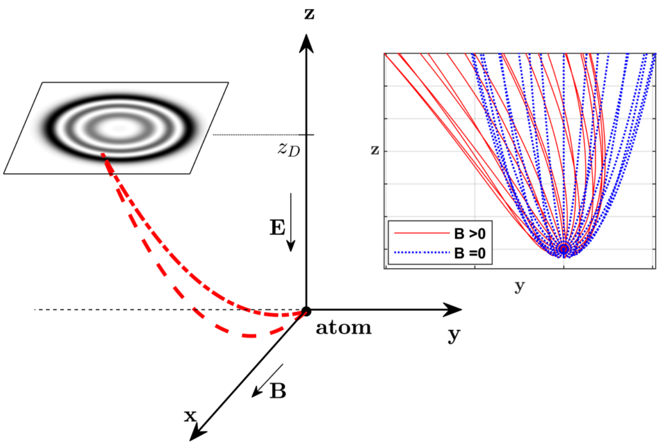

FIG. 2. Schematic representation for the photodetachment microscopy in a Cartesian system. Red lines (dashed and dot-dashed) indicate that there are two trajectories linking the atom to a final position in the detection screen. In the inset, classical trajectories are followed by the photodetached electron in the yz plane. Dotted blue lines are the trajectories in the case in which there is no magnetic field present. Red lines correspond to electron trajectories when a transverse magnetic field is present.

from the ion (source) placed at $\mathbf{r}_0 = x_0\,\hat{\imath} + y_0\,\hat{\jmath} + z_0\,\hat{\mathbf{k}}$ at initial time $t_0 = 0$ to the detection plane $z = z_D$ after a time of flight T. Figure 2 shows a scheme for this configuration within a Cartesian system. The classical motion of the electron is determined by the Lorentz force

$$\mathbf{F} = -q(\mathbf{E} + \mathbf{v} \times \mathbf{B}), \tag{3}$$

where $\mathbf{v}$ denotes the velocity of the electron. However, for the purpose of the description of the classical motion, we proceed within the Lagrangian formalism. In rectangular coordinates the Lagrangian $\mathcal{L}(\mathbf{r}, \dot{\mathbf{r}}; t)$ of an electron interacting with static electric and magnetic fields is given by

$$\mathcal{L}(\mathbf{r}, \dot{\mathbf{r}}; t) = \frac{m}{2}(\dot{x}^2 + \dot{y}^2 + \dot{z}^2) + q(\Phi - \mathbf{A} \cdot \dot{\mathbf{r}}). \tag{4}$$

The electric potential is $\Phi = Ez$ and the magnetic vector potential in the Coulomb gauge is $\mathbf{A} = \frac{1}{2}\mathbf{B} \times \mathbf{r} = \frac{B}{2}(-z\,\hat{\jmath} + y\,\hat{\mathbf{k}})$. Then, we can rewrite the Lagrangian as

$$\mathcal{L}(\mathbf{r}, \dot{\mathbf{r}}; t) = \frac{m}{2}[\dot{x}^2 + \dot{y}^2 + \dot{z}^2 + \omega(z\dot{y} - y\dot{z}) + 2\gamma z], \tag{5}$$

where we have introduced the cyclotron frequency $\omega = {}^{qB}/_{m}$ and the electron acceleration $\gamma = {}^{qE}/_{m}$.

From the Euler-Lagrange equations, the motion of the electron in the Cartesian system is determined by

$$x(t) = x_0 + v_{0,x}t, \tag{6a}$$

$$y(t) = y_0 - \frac{\gamma t}{\omega} + \frac{\gamma}{\omega^2}\sin(\omega t) + \frac{v_{0,y}}{\omega}\sin(\omega t) - \frac{2v_{0,z}}{\omega}\sin^2({}^{\omega t}/_{2}), \tag{6b}$$

$$z(t) = z_0 + \frac{2\gamma}{\omega^2}\sin^2({}^{\omega t}/_{2}) + \frac{2v_{0,y}}{\omega}\sin^2({}^{\omega t}/_{2}) + \frac{v_{0,z}}{\omega}\sin(\omega t). \tag{6c}$$

Furthermore, the canonical momentum $\mathbf{p} = m\dot{\mathbf{r}} - q\mathbf{A}$ can be directly computed. It gives

$$p_x(t) = mv_{0,x}, \tag{7a}$$

$$p_y(t) = \frac{m\omega}{2}z_0 - \frac{m\gamma}{\omega}\sin^2({}^{\omega t}/_{2}) + mv_{0,y}\cos^2({}^{\omega t}/_{2}) - \frac{mv_{0,z}}{2}\sin(\omega t), \tag{7b}$$

$$p_z(t) = -\frac{m\omega}{2}y_0 + \frac{m\gamma}{2}\left(t + \frac{\sin(\omega t)}{\omega}\right) + \frac{mv_{0,y}}{2}\sin(\omega t) + mv_{0,z}\cos^2({}^{\omega t}/_{2}). \tag{7c}$$

The initial velocity $\mathbf{v}_0 = v_{0,x}\,\hat{\imath} + v_{0,y}\,\hat{\jmath} + v_{0,z}\,\hat{\mathbf{k}}$ can be conveniently written in spherical coordinates (v_0, θ, ϕ) as

$$v_{0,x} = v_0\sin(\theta)\cos(\phi),$$
$$v_{0,y} = v_0\sin(\theta)\sin(\phi),$$
$$v_{0,z} = v_0\cos(\theta),$$

with v_0 the initial speed and the angles $0 \leqslant \theta < \pi$, $0 \leqslant \phi < 2\pi$ determine the initial orientation of the photoelectron. The classical trajectories followed by the electron are shown in Fig. 2 for different initial emission angles (θ, ϕ). A global drift of the trajectories along the $\mathbf{E} \times \mathbf{B}$ direction is observed when they are compared with the case with no magnetic field, as a result of the Lorentz force.

Since the electron must reach the detection plane at z_D, from Eq. (6c) we can clear the time the electron needs to reach the detector as a function of the initial releasing direction (θ, ϕ), assuming that $\omega t < \pi\ \forall t$; then

$$t_f(\theta, \phi) = \frac{1}{\omega}\arccos\left[\frac{\gamma + \omega v_0\sin(\theta)\sin(\phi) - \omega^2(z_D - z_0)}{\sqrt{[\gamma + \omega v_0\sin(\theta)\sin(\phi)]^2 + [\omega v_0\cos(\theta)]^2}}\right] - \frac{1}{\omega}\arctan\left[\frac{\omega v_0\cos(\theta)}{\gamma + \omega v_0\sin(\theta)\sin(\phi)}\right]. \tag{8}$$

Thus a parametrization of the path of the charged particle as a function of its emission angles, initial speed, and temporal variable can be theoretically available. However, the emission angles (θ, ϕ) are not accessible in the realization of the experiment. Instead, in experiments, the electron travels from a known initial position $\mathbf{r}_0$ to an observed final point $\mathbf{r}_f$ on the detector. Hamilton-Jacobi theory is more suitable dealing with paths defined by such initial and final conditions. Therefore, we change our point of view and alternatively treat the problem of the electron in crossed electric and magnetic fields within this framework. We start with the classical action functional $\mathcal{S}(\mathbf{r}, \mathbf{r}_0; T)$ that is minimized by classical paths

$$\mathcal{S}(\mathbf{r}, \mathbf{r}_0; T) = \int_0^T dt\,\mathcal{L}(\mathbf{r}, \dot{\mathbf{r}}; t). \tag{9}$$

In order to integrate the Lagrangian, Eq. (5), it is convenient to rewrite the particle trajectory Eq. (6) in terms of the quantities that remain constant in the course of the variation of the classical action. We express the components of initial velocity as a function of the initial position $\mathbf{r}_0$, the final position (the detector) $\mathbf{r}_f = x_f\,\hat{\mathbf{\imath}} + y_f\,\hat{\mathbf{\jmath}} + z_D\,\hat{\mathbf{k}}$, and the time of flight T the electron spends between $\mathbf{r}_0$ and $\mathbf{r}_f$,

$$v_{0,x} = \frac{x_f - x_0}{T}, \tag{10a}$$

$$\begin{aligned} v_{0,y} = {}& \frac{\omega}{2}[z_D - z_0 + (y_f - y_0)\cot({}^{\omega T}\!/_2)] \\ & - \frac{\gamma}{\omega}\left(1 - \frac{\omega T}{2}\cot({}^{\omega T}\!/_2)\right), \end{aligned} \tag{10b}$$

$$\begin{aligned} v_{0,z} = {}& -\frac{\gamma T}{2} - \frac{\omega}{2}(y_f - y_0) \\ & + \frac{\omega}{2}(z_D - z_0)\cot({}^{\omega T}\!/_2). \end{aligned} \tag{10c}$$

Replacing Eqs. (10) in the equations of motion (6), and then into Eq. (5) and finally integrating allows us to obtain the propagator

$$\begin{aligned} \mathcal{S}(\mathbf{r}_f, \mathbf{r}_0; T) = {}& \frac{m}{2T}(x_f - x_0)^2 \\ & + \frac{m\omega}{4}\cot({}^{\omega T}\!/_2)[(y_f - y_0)^2 + (z_D - z_0)^2] \\ & - \frac{m\gamma}{\omega}\left(1 - \frac{\omega T}{2}\cot({}^{\omega T}\!/_2)\right)(y_f - y_0) \\ & + \frac{m\gamma T}{2}(z_f + z_0) + \frac{m\omega}{2}(z_0 y_f - y_0 z_D) \\ & - \frac{m\gamma^2 T}{2\omega^2}\left(1 - \frac{\omega T}{2}\cot({}^{\omega T}\!/_2)\right). \end{aligned} \tag{11}$$

This propagator presents a natural link between quantum and classical mechanics [30–33].

Since the potential energy is time independent, for a given trajectory $\mathbf{r}(t)$ the electron energy $\mathcal{E}$ is conserved, and we may simplify the expression for the classical action by introducing the Hamilton's characteristic function $\mathcal{W}(\mathbf{r}_f, \mathbf{r}_0; \mathcal{E})$ via the Legendre transformation

$$\mathcal{S}(\mathbf{r}_f, \mathbf{r}_0; T) = \mathcal{W}(\mathbf{r}_f, \mathbf{r}_0; \mathcal{E}) - \mathcal{E}T. \tag{12}$$

In this way the total energy $\mathcal{E}$ can be obtained out of the classical action as $\mathcal{E}(\mathbf{r}_f, \mathbf{r}_0; T) = -{}^{\partial\mathcal{S}}\!/_{\partial T}$; it casts

$$\begin{aligned} \mathcal{E}(\mathbf{r}_f, \mathbf{r}_0; T) = {}& -m\gamma z_0 + \frac{m}{2T^2}(x_f - x_0)^2 + \frac{m\omega^2}{8}\csc^2({}^{\omega T}\!/_2) \\ & \times \left[\left(y_f - y_0 - \frac{\gamma}{\omega^2}[\sin(\omega T) - \omega T]\right)^2 \right. \\ & \left. + \left(z_D - z_0 - \frac{2\gamma}{\omega^2}\sin^2({}^{\omega T}\!/_2)\right)^2\right]. \end{aligned} \tag{13}$$

Since near-threshold photodetachment of negative ions provides an electron with sharply defined energy $\mathcal{E}$, rather than the times of flight T to reach the detector, only those trajectories fulfilling Eq. (13) are allowed. This transcendental equation needs to be solved numerically for the times of flight $T_j(\mathbf{r}_f, \mathbf{r}_0; \mathcal{E})$ provided that the total energy is $\mathcal{E} = {}^{mv_0^2}\!/_2 - m\gamma z_0$; here j labels the number of trajectories found. As a result, the Hamilton's characteristic function will not be unique, but has j branches depending on the choice of the trajectory,

$$\begin{aligned} \mathcal{W}_j(\mathbf{r}_f, \mathbf{r}_0; \mathcal{E}) = {}& \mathcal{S}(\mathbf{r}_f, \mathbf{r}_0; T_j(\mathbf{r}_f, \mathbf{r}_0; \mathcal{E})) \\ & + \mathcal{E}\,T_j(\mathbf{r}_f, \mathbf{r}_0; \mathcal{E}). \end{aligned} \tag{14}$$

A. Caustic surface

We need to study the formation of caustics due to the photodetached electron trajectories. The caustic is the surface enveloping the family of classical trajectories emitted in any possible direction. Due to the singularities at the caustic boundaries between classically allowed and classically forbidden events, a poor behavior from a primitive semiclassical description of the wave function is generally obtained near that surface [17,18,34]. In the time-of-flight picture, the points on the caustic surface Σ are such that they match the particle energy and, additionally, the energy as a function of T reaches a minimum there. Thus $\mathbf{r}_\Sigma$ is on the caustic surface if the two following equations,

$$\frac{\partial\mathcal{S}(\mathbf{r}_\Sigma, \mathbf{r}_0; T)}{\partial T} = -\mathcal{E}, \qquad \frac{\partial^2\mathcal{S}(\mathbf{r}_\Sigma, \mathbf{r}_0; T)}{\partial T^2} = 0,$$

hold simultaneously. The first equation has been already shown, Eq. (13), and the second derivative of the classical action reads

$$\begin{aligned} \frac{\partial^2\mathcal{S}(\mathbf{r}, \mathbf{r}_0; T)}{\partial T^2} = {}& -\frac{m\gamma^2}{2\omega}\tan({}^{\omega T}\!/_2) + \frac{m(x - x_0)^2}{T^3} \\ & + \frac{m\omega^3}{8}\csc^2({}^{\omega T}\!/_2)\cot({}^{\omega T}\!/_2)\left[(z - z_0)^2\right. \\ & \left. + \left(y - y_0 - \frac{\gamma}{\omega^2}[2\tan({}^{\omega T}\!/_2) - \omega T]\right)^2\right]. \end{aligned} \tag{15}$$

However, in the field arrangement we are studying these two equations cannot be simplified to obtain an explicit equation for the caustic surface in configuration space. Therefore, we solved them numerically to get a qualitative description.

Figure 3 shows the projection on the yz plane of the caustic surface as an envelope of electron trajectories when the transverse magnetic field is present. From our numerical analysis of the classical trajectories, we have found that every arrival point on the detection plane is linked to the source by two classical trajectories, for instance, the trajectories labeled as 1 and 2 in the figure. We notice that only one of them will always reach the caustic surface and folds back. This illustrates the simplest case of caustic, the fold type, where the classical electron trajectories turn back. For this type of caustic, the inevitable divergence observed due to the coalescence of two classical trajectories can be accurately approximated by Airy functions [34].

B. Classically allowed region at the detection plane

Once the electrons are detached and travel through the region where the external fields are, they are measured on the plane $z = z_D$. As seen from the caustic surface, for given initial conditions of the electron and magnitudes of the fields,

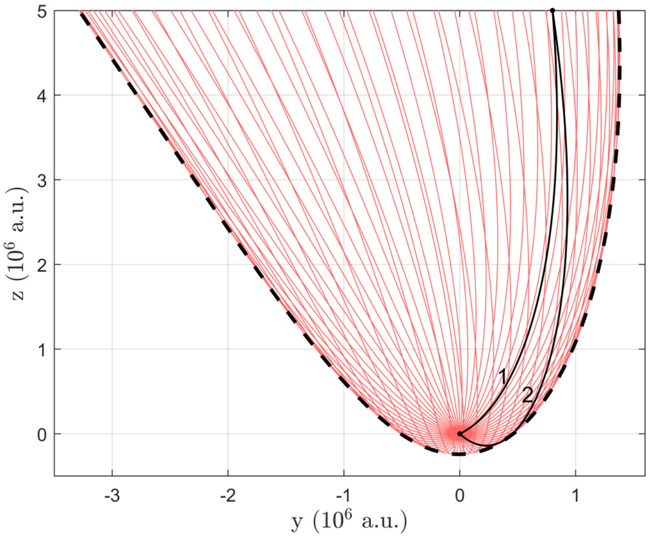

FIG. 3. Electron trajectories (thin red solid lines) projected on the yz plane when crossed electric and magnetic fields are present. The caustic surface is shown (thick black dashed line). Two classical trajectories reaching to one final point (black solid lines) are highlighted. Here, for the sake of the understanding and illustration, we have enhanced the effects by choosing $\mathcal{E} = 3.2$ meV, $E = 250$ V/m, and $B = 0.8$ mT.

there is a well-defined accessible region at the detection plane where the electron can classically arrive. From the classical analysis we can determine that region in the plane, i.e., the classically allowed region. The solution Eq. (6) leads to a clear distinction between a classically allowed region and a classically forbidden region.

In order to characterize the classically allowed region in the detection plane, we study the trajectories by means of Eq. (13). It is obtained that for the given initial energy $\mathcal{E}$ and field intensities at most two trajectories exist that connect the photoelectron initial position $\mathbf{r}_0$ and the detector at $\mathbf{r}_f$. On the other hand, for certain choice of final points no classical trajectory with real times of flight are found; this defines the classically forbidden region, later we will associate it as the quantum region, accessible by tunneling effect.

The characterization is performed replacing the known energy $\mathcal{E}$ in Eq. (13), such that we have

$$\left(\frac{2v_0}{\omega}\sin(^{\omega T}/_2)\right)^2 = \left(\frac{2}{\omega T}\sin(^{\omega T}/_2)(x_f - x_0)\right)^2 + \left(y_f - y_0 - \frac{\gamma}{\omega^2}[\sin(\omega T) - \omega T]\right)^2 + \left(z_D - z_0 - \frac{2\gamma}{\omega^2}\sin^2(^{\omega T}/_2)\right)^2, \quad (16)$$

which can be related to a conic section at $z = z_D$; specifically, an ellipse. At the detection plane the maximal radial extension occurs for nearly perpendicular emission of photoelectrons, i.e., $\theta \simeq {}^{\pi}/_2$, provided that the detector is placed farther than any atomic scale $\mathcal{E}/m\gamma \ll z_D - z_0$. Combining Eqs. (6) and (8), we get

$$x(\phi) \approx x_0 + \frac{2v_0}{\omega}\cos(\phi)\arcsin\left[\omega\sqrt{\frac{z_D - z_0}{2[\gamma + v_0\omega\,\sin(\phi)]}}\right], \quad (17)$$

$$y(\phi) \approx y_0 - \frac{2\gamma}{\omega^2}\arcsin\left[\omega\sqrt{\frac{z_D - z_0}{2[\gamma + v_0\omega\,\sin(\phi)]}}\right] + \frac{\sqrt{z_D - z_0}}{\omega}\sqrt{2[\gamma + v_0\omega\,\sin(\phi)] - \omega^2(z_D - z_0)}. \quad (18)$$

Therefore, varying the azimuthal angle ϕ we can describe the contour of the ellipse, which in the following we will refer to as the classical boundary for the electron trajectories.

The equation of the ellipse describing the classically allowed region at the detection plane is

$$\frac{(x - x_c)^2}{R_x^2} + \frac{(y - y_c)^2}{R_y^2} = 1, \quad (19)$$

where the coordinates of the center of the ellipse, from Eqs. (17) and (18), are given by

$$x_c \approx \frac{x(0) + x(\pi)}{2}, \qquad y_c \approx \frac{y\left(\frac{\pi}{2}\right) + y\left(\frac{3\pi}{2}\right)}{2}, \quad (20)$$

which explicitly read

$$x_c \simeq x_0, \quad (21)$$

$$y_c \simeq y_0 + \frac{1}{2\omega}(\mathcal{A}_+ + \mathcal{A}_-) - \frac{\gamma}{\omega^2}(\arcsin[\mathcal{B}_+] + \arcsin[\mathcal{B}_-]). \quad (22)$$

Instead the principal radii are obtained from

$$R_x \approx \frac{x(0) - x(\pi)}{2}, \qquad R_y \approx \frac{y\left(\frac{\pi}{2}\right) - y\left(\frac{3\pi}{2}\right)}{2}, \quad (23)$$

which cast

$$R_x \simeq \frac{2v_0}{\omega}\arcsin\left[\omega\sqrt{\frac{z_D - z_0}{2\gamma}}\right], \quad (24)$$

$$R_y \simeq \frac{1}{2\omega}(\mathcal{A}_+ - \mathcal{A}_-) + \frac{\gamma}{\omega^2}\arcsin\left[\frac{\omega}{2\sqrt{\gamma^2 - v_0^2\omega^2}}(\mathcal{A}_+ - \mathcal{A}_-)\right]. \quad (25)$$

The following functions have been introduced:

$$\mathcal{A}_+ = \sqrt{2(\gamma + v_0\omega)(z_D - z_0) - \omega^2(z_D - z_0)^2}, \quad (26)$$

$$\mathcal{A}_- = \sqrt{2(\gamma - v_0\omega)(z_D - z_0) - \omega^2(z_D - z_0)^2}, \quad (27)$$

$$\mathcal{B}_+ = \omega\sqrt{\frac{z_D - z_0}{2(\gamma + \omega v_0)}}, \quad (28)$$

$$\mathcal{B}_- = \omega\sqrt{\frac{z_D - z_0}{2(\gamma - \omega v_0)}}. \quad (29)$$

For a fully geometrical parametrization of the classically allowed region of the photodetachment electron at the detector

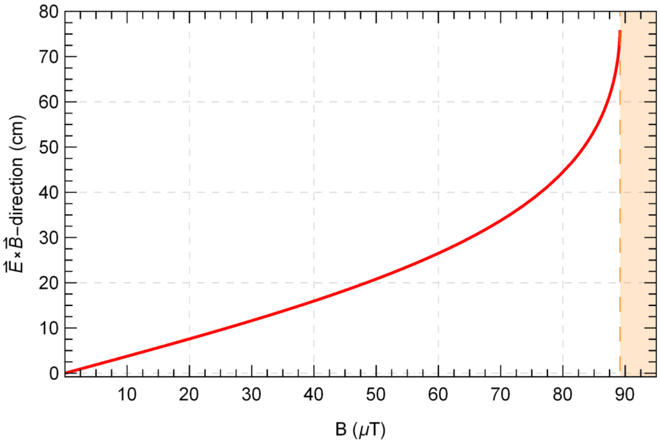

FIG. 4. Calculated geometric center along the $\mathbf{E}\times\mathbf{B}$ direction of the spatial electron distribution in the detection plane for near-threshold photodetachment microscopy as a function of the intensity of a transverse magnetic field (red line). Vertical orange dashed line indicates $B_{\max}$. Shadowed orange region highlights the forbidden B-field intensities.

we can compute its eccentricity

$$e=\sqrt{1-(R_x/R_y)^2}. \tag{30}$$

It is worth mentioning that, in the limit $\omega\to 0$, corresponding to no magnetic field, all these results converge to the known results for the standard photodetachment microscopy [6,13].

From all the above, for a meaningful physical interpretation of those quantities we require that they have to be real. The classical analysis of the arrival region at the detector allows us to set an upper limit for the intensity of the magnetic field. In terms of the controlled parameters the intensity of the field must be such that

$$B\leqslant\frac{\sqrt{2m}}{q(z_D-z_0)}(\sqrt{\mathcal{E}+m\gamma z_D}-\sqrt{\mathcal{E}+m\gamma z_0}). \tag{31}$$

The right-hand side on the equation above fixes the maximum value of the magnetic field, $B_{\max}$. Since $\mathcal{E}/m\gamma(z_D-z_0)\ll 1$, we can further approximate

$$B_{\max}\approx\frac{m}{q}\sqrt{\frac{2\gamma}{z_D-z_0}}\left(1-\sqrt{\frac{z_0}{z_D-z_0}+\frac{\mathcal{E}}{m\gamma(z_D-z_0)}}\right). \tag{32}$$

Following a primitive analysis of the electron dynamics we have fully characterized the arrival region at the detection plane $z=z_D$. Given the initial photoelectron energy, the magnitude of the electric field, and the position of the detector in the configuration shown in Fig. 2, the intensity of the transverse magnetic field must be $B<B_{\max}$; otherwise, the electron does not reach the detection plane at z_D and no electron is detected. For the set of values we have fixed for our studies, see Sec. II, $B_{\max}\approx 89.16\ \mu$T.

Additionally, we have seen that the geometric center of the classically allowed region varies along the $\mathbf{E}\times\mathbf{B}$ direction, Eq. (22), as a function of the intensity of the field. Figure 4 shows the center position, y_c, versus the magnetic field. Notice that the maximum displacement of the center is bounded by $B_{\max}$. As theoretically calculated, in near-threshold photodetachment microscopy, the region where the spatial electron distribution is recorded has an elliptic shape and its properties depend on the magnitude of the magnetic field. Figure 5 shows the variation of the principal radii R_x and R_y as a function of the magnetic-field intensity and the eccentricity calculated from Eq. (30). We notice that R_x does not vary significantly with B, while R_y does. This indicates that the spatial electron distribution is not only displaced along the $\mathbf{E}\times\mathbf{B}$ direction, but its shape is also elongated along it. In the particular set of magnitudes considered, we see that $R_x\sim R_y$ up to 20 μT; in consequence the shape of the classically allowed region will look circular, eccentricity $e\sim 0.3$. For higher intensities the difference between the two principal axes becomes greater and the elliptic shape becomes evident. The quantitative analysis indicates that the eccentricity e may take any value from zero (when $B=0$) to close to but less than one (when $B\to B_{\max}$). All these clearly determine the contour of the shape of the electron distribution in the detection plane.

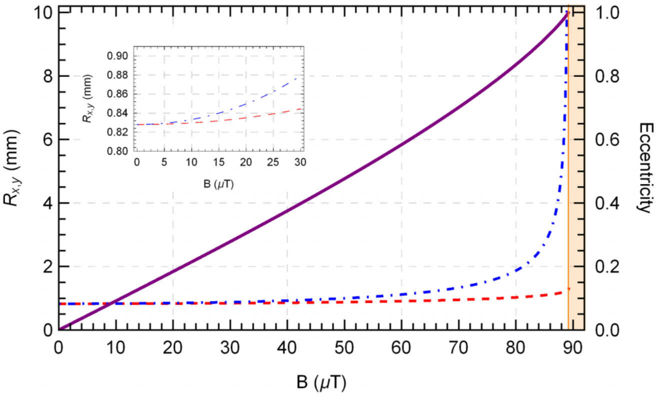

FIG. 5. Radii along the principal axes and eccentricity of the classically allowed region in the xy plane on the detector as a function of the transverse magnetic-field intensity. In the left axis, the variation of the radii, R_x (red dashed line) and R_y (blue dot-dashed line), are represented and, in the right axis, the calculated eccentricity (solid purple line). The inset shows the variation of the radii, R_x and R_y, for weaker intensities to highlight when they become distinguishable. Vertical orange line at $B_{\max}$ determines the upper limit of magnetic-field intensity.

IV. APPROXIMATION OF QUANTUM SOURCE THEORY

In the quantum description of the photodetachment process we can replace the photon-ion interaction by an electron-generating mechanism, a source that emits electrons with proper angular characteristics. This is the so-called quantum source theory [20,21,35,36]. Within this treatment, the motion of the electrons in the static fields is governed by the inhomogeneous stationary Schrödinger equation

$$(\mathcal{E}-\mathcal{H}_{\rm qst})\psi(\mathbf{r})=\sigma(\mathbf{r}), \tag{33}$$

where $\sigma(\mathbf{r})$ describes the source of electrons and $\mathcal{H}_{\rm qst}$ is the Hamilton operator governing the dynamics of the detached electron; it can be decomposed as $\mathcal{H}_{\rm qst}=\mathcal{H}+\mathcal{V}$. The first term, $\mathcal{H}$, stands for the canonical quantification of the Hamiltonian obtained from the Legendre transformation of the Lagrangian Eq. (5),

$$\mathcal{H} = \frac{d\mathbf{r}}{dt}\cdot\mathbf{p} - \mathcal{L} = \frac{1}{2m}(\mathbf{p}+q\mathbf{A})^2 - q\,\Phi(\mathbf{r}), \tag{34}$$

whereas the second term $\mathcal{V}$ describes the interaction with the remaining neutral atomic core.

We introduce the energy-Green function $\mathcal{G}(\mathbf{r},\mathbf{r}_0;\mathcal{E})$, such that $(\mathcal{E}-\mathcal{H}_{\mathrm{qst}})\mathcal{G}(\mathbf{r},\mathbf{r}_0;\mathcal{E}) = \delta(\mathbf{r}-\mathbf{r}_0)$. A solution for the electron wave function in terms of the convolution integral reads

$$\psi(\mathbf{r}) = \int d^3r'\,\mathcal{G}(\mathbf{r},\mathbf{r}';\mathcal{E})\sigma(\mathbf{r}'). \tag{35}$$

The theory of quantum sources becomes particularly simple for point sources and that is the first approximation we use. For a pointlike source at $\mathbf{r_0}$ (which later we will resume as the origin of the coordinate system), such that $\sigma(\mathbf{r})\sim\delta(\mathbf{r}-\mathbf{r}_0)$, the electron wave function $\psi(\mathbf{r})$ is just proportional to the energy-Green function $\mathcal{G}(\mathbf{r},\mathbf{r}_0;\mathcal{E})$ itself. This approximation is justified in near-threshold scattering $\mathcal{E}\to 0$, since the emerging wave effectively obliterates the internal structure of the source. However, this leads to isotropic emissions, i.e., *s* waves, whereas the source in practice might provide photodetached electrons with nonzero angular momentum. In order to take into account multipole waves a description by analogy with the multipole formalism commonly used in potential theory has been introduced [37].

The internal orbital structure of the pointlike sources is imprinted onto the energy-Green function by means of the spherical tensor gradient. This follows from the definition of the multipole point sources $\delta_{lm}(\mathbf{r}-\mathbf{r}_0)$ via the spherical delta functions [38]

$$\delta_{lm}(\mathbf{r}-\mathbf{r}_0) = \mathcal{Y}_{lm}(\boldsymbol{\nabla}_0)\delta(\mathbf{r}-\mathbf{r}_0), \tag{36}$$

where $\mathcal{Y}_{lm}(\boldsymbol{\nabla}_0)$ is the spherical tensor gradient given by [39,40]

$$\begin{aligned}\mathcal{Y}_{lm}(\boldsymbol{\nabla}_0) = {}&\left[\frac{2l+1}{4\pi}(l+m)!(l-m)!\right]^{1/2}\\ &\times\sum_{\nu\geqslant 0}\frac{\left(-\partial_{x_0}-i\,\partial_{y_0}\right)^{m+\nu}\left(\partial_{x_0}-i\,\partial_{y_0}\right)^{\nu}\left(\partial_{z_0}\right)^{l-m-2\nu}}{2^{m+2\nu}(m+\nu)!\,\nu!\,(l-m-2\nu)!}.\end{aligned} \tag{37}$$

Notice that the differentiation proceeds with respect to the Cartesian coordinates of the source position $\mathbf{r}_0$.

Then, the inhomogeneous Schrödinger equation for the multipoles $(\mathcal{E}-\mathcal{H}_{\mathrm{qst}})\mathcal{G}_{lm}(\mathbf{r},\mathbf{r}_0;\mathcal{E}) = \delta_{lm}(\mathbf{r}-\mathbf{r}_0)$ is formally solved by the multipole Green functions $\mathcal{G}_{lm}(\mathbf{r},\mathbf{r}_0;\mathcal{E})$, which are available from $\mathcal{G}(\mathbf{r},\mathbf{r}_0;\mathcal{E})$ by differentiation

$$\mathcal{G}_{lm}(\mathbf{r},\mathbf{r}_0;\mathcal{E}) = \mathcal{Y}_{lm}(\boldsymbol{\nabla}_0)\,\mathcal{G}(\mathbf{r},\mathbf{r}_0;\mathcal{E}). \tag{38}$$

Thus the resulting electron wave function with orbital angular momentum l and magnetic number m is simply

$$\psi_{lm}(\mathbf{r}) \propto \mathcal{G}_{lm}(\mathbf{r},\mathbf{r}_0;\mathcal{E}). \tag{39}$$

Here, we focus our attention on the case of *s* waves and *p* waves, so that the corresponding multipole Green function can be obtained from Eq. (37) and Eq. (38) by

$$\mathcal{G}_{00}(\mathbf{r},\mathbf{r}_0;\mathcal{E}) = \sqrt{\frac{1}{4\pi}}\,\mathcal{G}(\mathbf{r},\mathbf{r}_0;\mathcal{E}), \tag{40}$$

$$\mathcal{G}_{10}(\mathbf{r},\mathbf{r}_0;\mathcal{E}) = \sqrt{\frac{3}{4\pi}}\,\frac{\partial}{\partial z_0}\mathcal{G}(\mathbf{r},\mathbf{r}_0;\mathcal{E}), \tag{41}$$

$$\mathcal{G}_{1\pm1}(\mathbf{r},\mathbf{r}_0;\mathcal{E}) = \mp\sqrt{\frac{3}{8\pi}}\left(\frac{\partial}{\partial x_0}\pm i\frac{\partial}{\partial y_0}\right)\mathcal{G}(\mathbf{r},\mathbf{r}_0;\mathcal{E}). \tag{42}$$

Thereupon we address our attention to determine the isotropic energy-Green function $\mathcal{G}(\mathbf{r},\mathbf{r}_0;\mathcal{E})$. The second main approximation arises from ignoring the interaction of the photodetached electron with the remaining atom, i.e., $\mathcal{V}\to 0$. Therefore, the energy-Green function is computed only for the interaction with the external fields governing the electron motion. We introduce the time-dependent quantum propagator $K(\mathbf{r},\mathbf{r}_0;T)$, which is determined by the action functional $\mathcal{S}(\mathbf{r},\mathbf{r}_0;T)$ through the path-integral formulation of quantum mechanics [30,32,33]

$$K(\mathbf{r},\mathbf{r}_0,T) = \sqrt{\det\left[\frac{i}{2\pi\hbar}\frac{\partial^2\mathcal{S}}{\partial\mathbf{r}\partial\mathbf{r}_0}\right]}\exp\left[\frac{i}{\hbar}\mathcal{S}(\mathbf{r},\mathbf{r}_0;T)\right]. \tag{43}$$

Given the action, Eq. (9), we can write [21,41,42]

$$\begin{aligned}K(\mathbf{r},\mathbf{r}_0,T) = {}&\frac{m\omega}{4\pi i\hbar}\sqrt{\frac{m}{2\pi i\hbar T\,\sin^2(\omega T/2)}}\\ &\times\exp\left[\frac{i}{\hbar}\mathcal{S}(\mathbf{r},\mathbf{r}_0;T)\right].\end{aligned} \tag{44}$$

Then, the energy-Green function can be obtained via the Laplace transformation

$$\mathcal{G}(\mathbf{r},\mathbf{r}_0;\mathcal{E}) = \frac{1}{i\hbar}\int_0^\infty dT\,e^{i\mathcal{E}T/\hbar}K(\mathbf{r},\mathbf{r}_0;T). \tag{45}$$

However, this integral cannot be solved in a closed form analytically and an exact numerical evaluation results demanding efforts beyond our scope. Therefore, in order to evaluate it, we use the stationary phase approximation together with the uniform Airy approximation to overcome the divergences at the classical boundary [13,17,18,34]. The phase in Eq. (45) is given by $[\mathcal{E}T+\mathcal{S}(\mathbf{r},\mathbf{r}_0;T)]/\hbar$, which is proportional to the Hamilton characteristic function, Eq. (14). We have already determined that, for every final position $\mathbf{r}_f$, the phase has two stationary points in the classically allowed region, say T_1 and T_2, the solutions of Eq. (13). They satisfy $T_1 < T_2$; see Fig. 3. This notation is chosen in such a way that T_1 and T_2 correspond to a phase minima and phase maxima, respectively; i.e., $\partial^2\mathcal{S}/\partial T^2|_{T_1} > 0$ and $\partial^2\mathcal{S}/\partial T^2|_{T_2} < 0$. Hence the energy-Green function that remains finite at the coalescence points on the classical boundary is given by

$$\mathcal{G}(\mathbf{r}_f,\mathbf{r}_0;\mathcal{E}) = \mathcal{C}(\mathcal{O}_+\zeta^{1/4}\mathrm{Ai}(-\zeta) - i\mathcal{O}_-\zeta^{-1/4}\mathrm{Ai}'(-\zeta)), \tag{46}$$

where the Airy function $\mathrm{Ai}(-\zeta)$ appears explicitly, as well as its derivative $\mathrm{Ai}'(-\zeta) = d\mathrm{Ai}(-\zeta)/d(-\zeta)$ [43]. Accordingly, we have also introduced

$$\zeta = \left(\frac{3}{4\hbar}(\mathcal{W}_2 - \mathcal{W}_1)\right)^{2/3}. \tag{47}$$

For a shorter notation $\mathcal{W}_j = \mathcal{S}(\mathbf{r}_f, \mathbf{r}_0; T_j(\mathbf{r}_f, \mathbf{r}_0; \mathcal{E})) + \mathcal{E}\, T_j(\mathbf{r}_f, \mathbf{r}_0; \mathcal{E})$. Also the functions

$$\mathcal{C} = \frac{m\omega}{4\hbar^2}\sqrt{\frac{m}{i\pi}} \exp\left[\frac{i}{2\hbar}(\mathcal{W}_1 + \mathcal{W}_2)\right] \tag{48}$$

and

$$\mathcal{O}_\pm = \left(T_1 \sin^2(\omega T_1/2)\, \frac{\partial^2 \mathcal{S}}{\partial T^2}\bigg|_{T_1}\right)^{-1/2} \pm \left(-T_2 \sin^2(\omega T_2/2)\, \frac{\partial^2 \mathcal{S}}{\partial T^2}\bigg|_{T_2}\right)^{-1/2}. \tag{49}$$

Notice that, in Eq. (49), appears Eq. (15) evaluated at T_1 and T_2.

Once we have Eq. (46), we can compute the corresponding electron wave function via the energy-Green function for s waves and p waves. We immediately notice that for s waves Eq. (46) differs from Eq. (40) only by a factor $1/\sqrt{4\pi}$. Instead, for p waves differentiation with respect to the coordinates of the initial (source) position are needed, Eqs. (41) and (42). We have found that those derivatives can, in short, be written as

$$\frac{\partial \mathcal{G}(\mathbf{r}_f, \mathbf{r}_0; \mathcal{E})}{\partial r_0} = \frac{1}{2\hbar}\mathcal{C}\big(\mathcal{D}_{+,r_0}\, \zeta^{1/4}\, \mathrm{Ai}(-\zeta) - i\,\mathcal{D}_{-,r_0}\, \zeta^{-1/4}\, \mathrm{Ai}'(-\zeta)\big). \tag{50}$$

The coefficients introduced here are

$$\mathcal{D}_{+,r_0} = 2\hbar\frac{\partial \mathcal{O}_+}{\partial r_0} + \left(\frac{\mathcal{O}_+}{4\zeta^{3/2}} + i(\mathcal{O}_+ - \mathcal{O}_-)\right)\frac{\partial \mathcal{W}_2}{\partial r_0} - \left(\frac{\mathcal{O}_+}{4\zeta^{3/2}} - i(\mathcal{O}_+ + \mathcal{O}_-)\right)\frac{\partial \mathcal{W}_1}{\partial r_0}, \tag{51a}$$

$$\mathcal{D}_{-,r_0} = 2\hbar\frac{\partial \mathcal{O}_-}{\partial r_0} - \left(\frac{\mathcal{O}_-}{4\zeta^{3/2}} + i(\mathcal{O}_+ - \mathcal{O}_-)\right)\frac{\partial \mathcal{W}_2}{\partial r_0} + \left(\frac{\mathcal{O}_-}{4\zeta^{3/2}} + i(\mathcal{O}_+ + \mathcal{O}_-)\right)\frac{\partial \mathcal{W}_1}{\partial r_0}. \tag{51b}$$

By appropriate substitution of r_0 by any of the initial Cartesian coordinates x_0, y_0, z_0, we can straightforwardly construct the wave functions, Eq. (39), according to Eqs. (41) and (42). In the Appendix all the derivatives needed to compute the energy-Green function for p waves are shown.

V. CLOSED-ORBIT THEORY

On the other hand, a well established semiclassical approximation to the time-independent wave function is the closed-orbit theory [23,44,45]. In the same way, when the ion absorbs a photon the released electron propagates away from the atom to large distances; however, this approach takes into account that near the atomic core a semiclassical approximation cannot be applied. The standard procedure of the aforementioned approximation consists of dividing the space into two regions around the ion core (placed at the origin of a Cartesian system as in Fig. 2), namely inner and outer regions. We choose as the boundary a spherical surface of radius $R_s \sim 10$–$50a_0$, with a_0 the Bohr radius. Generally, the vector and electric potential are far smaller than the kinetic energy in the inner region. Therefore, the external fields can be reasonably neglected in this region, and the interaction with the remaining neutral atomic core ignored. Within these approximations the Hamiltonian in the inner region takes the form $\mathcal{H}_{\text{in}} = p^2/2m$. And the electron wave function must satisfy the inhomogeneous Schrödinger equation [46]

$$(\mathcal{E} - \mathcal{H}_{\text{in}})\psi_{\text{in}} = \mathcal{D}\varphi, \tag{52}$$

where $\mathcal{D}$ is the dipole operator accounting for the interaction with the laser, φ is the initial atom state, and $\mathcal{E}$ is the energy of the electron. The solution on the surface can be written as [47]

$$\psi_s(\mathbf{r}_s) = C(k_0)Y_{lm}(\theta, \phi)\frac{e^{ik_0R_s}}{R_s}, \tag{53}$$

with $C(k_0)$ a constant related to energy, the vector position $\mathbf{r}_s$ on the surface between the two regions is given by the set of spherical coordinates (R_s, θ, ϕ), and Y_{lm} are the spherical harmonics for quantum numbers l and m related to the angular momentum, as usual.

Meanwhile, in the outer region the electron wave function propagates according to semiclassical mechanics; therefore, it can be constructed with the classical trajectories $\mathbf{r}(\theta, \phi, t)$ obtained from Eqs. (6). Contrary to the analysis in Sec. IV where the initial position was considered to be the origin of the Cartesian system, same as the atom position, under the current circumstances, we consider the initial position $\mathbf{r}_0$ in Eqs. (6) to be the position of the electron on the boundary between the two regions $\mathbf{r}_s$, i.e., $(x_0, y_0, z_0) = [R_s\sin(\theta)\cos(\phi), R_s\sin(\theta)\sin(\phi), R_s\cos(\theta)]$. In a global asymptotic form the wave function is [27,44,45]

$$\psi(\mathbf{r}) = \sum_j \psi_s(\mathbf{r}_{s,j})A_j \exp\left[i\left(\frac{S_j}{\hbar} - \frac{\pi}{2}\mu_j\right)\right], \tag{54}$$

where the sum is over all the classical trajectories $\mathbf{r}(\theta, \phi, t)$ going from $\mathbf{r}_s$ on the limiting surface to the final position $\mathbf{r}$ on the detection plane; $S_j(\mathbf{r}, \mathbf{r}_s, t)$ is the time-dependent Hamilton's principal function. The classical trajectory family density along the jth trajectory is A_j. The Maslov index μ_j represents the relative phases of various terms in the superposition and it increases by one (for the particular fold caustic we face here) when A_j passes a singularity.

The Hamilton's principal function is given by

$$S_j(\mathbf{r}_f, \mathbf{r}_s, t_f) = S_0(\mathbf{r}_{s,j}) + \int_{\mathbf{r}_{s,j}}^{\mathbf{r}_f} \mathbf{p}_j \cdot d\mathbf{r}_j, \tag{55}$$

where $\mathbf{p}_j$ is the canonical momentum for the jth trajectory, Eq. (7). On the surface $S_0(\mathbf{r}_{s,j})$ must satisfy $dS_0(\mathbf{r}_{s,j}) = \mathbf{p}_{s,j} \cdot \mathbf{r}_{s,j}$; therefore,

$$dS_0(\mathbf{r}_{s,j}) = \frac{m\omega}{2}R_s^2[\sin(\theta_j)\cos(\theta_j)\cos(\phi_j)d\phi + \sin(\theta_j)d\theta],$$

which can be safely neglected. From Eq. (6) and Eq. (7) we can write $S_j(\mathbf{r}_f, \mathbf{r}_s, t_f)$ as an expansion in terms of R_s as

$$S_j(\mathbf{r}_f, \mathbf{r}_s, t_f) = s_j^0 + s_j^1 R_s, \tag{56}$$

with

$$s_j^0 = \frac{mt_f}{2\omega^2}\left(\gamma^2 + v_0^2\omega^2\right) + \frac{mv_0^2}{2\omega}\cos^2(\phi_j)\sin^2(\theta_j)[\omega t_f - \sin(\omega t_f)]$$
$$+ \frac{m\gamma}{\omega^2}(2v_0\cos(\theta_j) + \gamma t_f + v_0\omega t_f\sin(\theta_j)\sin(\phi_j))\sin^2({}^{\omega t_f}\!/_2) - \frac{m}{2\omega^3}\left(\gamma^2 - v_0^2\omega^2 - v_0\omega^2\gamma t_f\cos(\theta_j)\right)\sin(\omega t_f), \quad (57)$$

$$s_j^1 = \frac{m}{2\omega}(\gamma[\sin(\omega t_f) - \omega t_f]\cos(\theta_j) - 2\sin^2({}^{\omega t_f}\!/_2)\{v_0\omega\cos^2(\theta_j) + [\gamma + v_0\omega\sin(\theta_j)\sin(\phi_j)]\sin(\theta_j)\sin(\phi_j)\}). \quad (58)$$

Meanwhile, for the density of classical trajectories A_j, we first need to define the Jacobian

$$J(t,\mathbf{r}) = \frac{\partial(x,y,z)}{\partial(t,\theta,\phi)} = \begin{vmatrix} {}^{\partial x}\!/_{\partial\theta} & {}^{\partial x}\!/_{\partial\phi} & {}^{\partial x}\!/_{\partial t} \\ {}^{\partial y}\!/_{\partial\theta} & {}^{\partial y}\!/_{\partial\phi} & {}^{\partial y}\!/_{\partial t} \\ {}^{\partial z}\!/_{\partial\theta} & {}^{\partial z}\!/_{\partial\phi} & {}^{\partial z}\!/_{\partial t} \end{vmatrix}, \quad (59)$$

from which in order of R_s we get

$$J(t,\theta,\phi) = \frac{v_0^2\sin(\theta)}{\omega^2}\left(j_o(t,\theta,\phi) + \frac{1}{v_0}j_1(t,\theta,\phi)R_s + \frac{\omega}{v_0^2}j_2(t,\theta,\phi)R_s^2\right) \quad (60)$$

and the coefficients are

$$j_o(t,\theta,\phi) = a(t,\theta,\phi)\sin(\omega t) + 4\,b(t,\theta,\phi)\sin^2({}^{\omega t}\!/_2),$$
$$j_1(t,\theta,\phi) = \omega\,a(t,\theta,\phi) + \omega[v_0 + b(t,\theta,\phi)]\sin(\omega t)$$
$$+ 2[2\gamma\ \cos(\theta) - \omega t\ c(\theta,\phi)]\sin^2({}^{\omega t}\!/_2),$$
$$j_2(t,\theta,\phi) = v_0\omega + \gamma\ \cos(\theta)\sin(\omega t) - 2\,c(\theta,\phi)\sin^2({}^{\omega t}\!/_2),$$

with

$$a(t,\theta,\phi) = v_0\omega t[1 - \sin^2(\theta)\cos^2(\phi)],$$
$$b(t,\theta,\phi) = \gamma t\ \cos(\theta) + v_0\sin^2(\theta)\cos^2(\phi),$$
$$c(\theta,\phi) = \gamma\ \sin(\theta)\sin(\phi) + v_0\omega[1 - \sin^2(\theta)\cos^2(\phi)].$$

Thus we may refer to the definition of the density of classical trajectories and compute it as

$$A_j = \left|\frac{J(0,\mathbf{r})}{J(t_f,\mathbf{r})}\right|^{1/2}. \quad (61)$$

Substituting, it takes the form

$$A_j \approx \frac{R_s\omega}{\sqrt{v_0}}(4\gamma t_f\cos(\theta_j)\sin^2({}^{\omega t_f}\!/_2)$$
$$+ 4v_0\cos^2(\phi_j)\sin^2(\theta_j)\sin^2({}^{\omega t_f}\!/_2)$$
$$+ v_0\omega t_f[1 - \sin^2(\theta_j)\cos^2(\phi_j)]\sin(\omega t_f))^{-1/2}, \quad (62)$$

where we have conveniently neglected terms $\propto R_s^2$ and higher. The time t_f is given in terms of (θ,ϕ) as in Eq. (8).

According to Sec. III A, for near-threshold photodetachment microscopy in the presence of a transverse magnetic field two trajectories connect each point in the detection plane with the source. Let us consider the two sets of initial emission angles, (θ_1,ϕ_1) and (θ_2,ϕ_2), which are obtained for the times of flight T_1 and T_2, Eq. (13), by numerically solving Eq. (8). Also, in this case, the two sets of emission angles determine the two classical trajectories arriving at the same point in the classically allowed region on the detector. We labeled as 1 the trajectory going to the detection plane without touching the caustic surface, while 2 is the one touching it; see Fig. 3. Then, the Maslov index takes the value $\mu_1 = 0$, and $\mu_2 = 1$, for any final point $\mathbf{r}_f$.

Finally, the primitive semiclassical approximation for the electron wave function at the final point $\mathbf{r}$ constructed from the closed orbit theory can be written as

$$\psi(\mathbf{r}) = C(k_0)\frac{\exp(ik_0R_s)}{R_s}[A_1Y_{lm}(\theta_1,\phi_1)e^{iS_1/\hbar}$$
$$+ A_2Y_{lm}(\theta_2,\phi_2)e^{i(S_2/\hbar - \pi/2)}]. \quad (63)$$

The divergence in this constructed wave function around caustics can be fixed by the application of the Airy uniform approximation [31,34].

VI. ELECTRON FLUX DISTRIBUTION

From the electron wave function the probability density and the probability current become easily accessible, and they can be linked to the two-dimensional spatial distribution usually recorded at the detector in experiments. This can be achieved by either of the two theoretical approaches used, namely quantum source theory and closed-orbit theory. Within the semiclassical formalism, the probability current along the normal component of the imaging detector, Eq. (2), can be consistently approximated as [16,37,48]

$$j_z = v_z\,|\psi(\mathbf{r})|^2, \quad (64)$$

with $v_z \approx \sqrt{(z_D - z_0)[2\gamma - \omega^2(z_D - z_0)]}$. The value of v_z can be considered as the same for every trajectory and final point since the electron is accelerated greatly by the static electric field along that direction.

In the interest of studying the effects of the initial angular distribution of the electrons, we explore the cases where the initial emitted electronic state corresponds to s waves and p waves, which could be associated to experiments with S^- and H^-, respectively. In Fig. 6, we compared the profile of the electron probability density obtained from the two theoretical approaches. It is worth remarking that, for improved accuracy near the boundary of the classically allowed region, we have used a uniform Airy approximation. The probability density profile was extended into the classically forbidden region, in

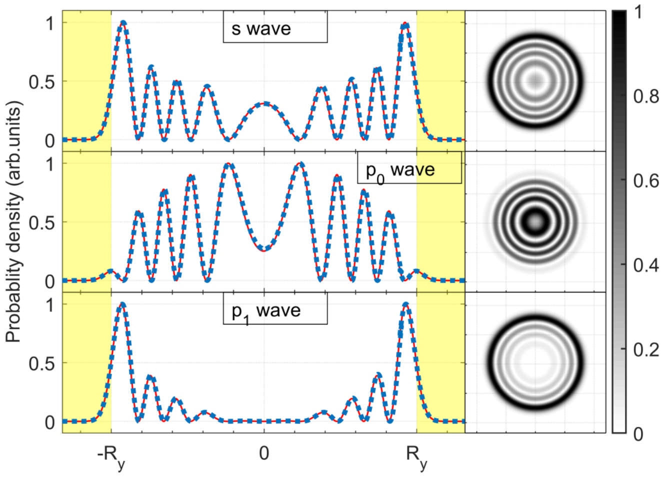

FIG. 6. Electron probability density profile along the positive y direction for different initial electron states and their corresponding calculated interference patterns. The result for an s wave ($l = 0$) is shown on the top panel, for the p wave identified as p_0 ($l = 1$ and $m = 0$) is in the middle, while in the bottom panel it is for p_1 ($l = 1$ and $m = \pm 1$). The solid red lines correspond to the solution from the closed-orbit theory, while the blue squares correspond to the energy-Green function method. The classically forbidden region has been shadowed in yellow. The physical parameters used correspond to $\mathcal{E} = 120\ \mu$eV, $E = 350$ V/m, and $B = 2\ \mu$T, and the detector placed at a distance $z_D = 0.5$ m; for those $R_y \approx 0.82$ mm.

yellow in the figure, by analytic continuation of its behavior near the boundary, i.e., we include the exponentially suppressed contributions of tunneling trajectories; interference is absent there. The results out of the two theoretical methods are virtually indistinguishable for any value of the orbital angular momentum and fields intensities studied. As seen also from the profile, the interference patterns show different inner structure depending on electronic orbital angular momentum and its magnetic number, albeit the classical boundary is independent of those initial conditions. Since both approaches show identical results, in the following we will show only the patterns obtained by the use of the closed-orbit theory which are numerically easier to access.

As obtained from the classical equations of motion the numerically simulated patterns show the same features as the experimental results in the presence of a transverse magnetic field: a global shift of the center of the distribution along the $\mathbf{E} \times \mathbf{B}$ direction depending on the field intensity [7]. As seen from Fig. 6, the ring distribution depends on the angular momentum of the detached electron, but its number, four for this particular set of values, remains the same. However, when the intensity of the magnetic field increases some other phenomena are observed [22]. We have previously determined the dependence of the position of the center of the interference pattern on the xy plane at z_D as a function of the strength of the magnetic field, Eqs. (21) and (22). Figure 7 depicts the changes of the shape of the interference pattern as a function of the B field; on top of those we have also drawn the variation of the center of the pattern, theoretically determined. Notice that for no magnetic field we obtain the known results: the two-dimensional spatial distribution is circular and centered at the atom position [5]. For weak intensities of the transverse field the interference pattern is drifted but qualitatively the pattern looks like a circle [7,22]. Meanwhile, for stronger intensities of the magnetic field the displacement of the pattern becomes larger, with a faster growing behavior when the intensity approaches $B_{\max}$. Under these circumstances we have shown the unambiguous change of the shape of the interference pattern: the pattern is elongated along the orthogonal direction of the magnetic field, i.e., y direction. From there we confirmed our classical findings: in absence of the B field the pattern is circular ($e = 0$), and then it becomes elliptical ($e \rightarrow 1$) as the magnetic field increases and reaches its maximum value.

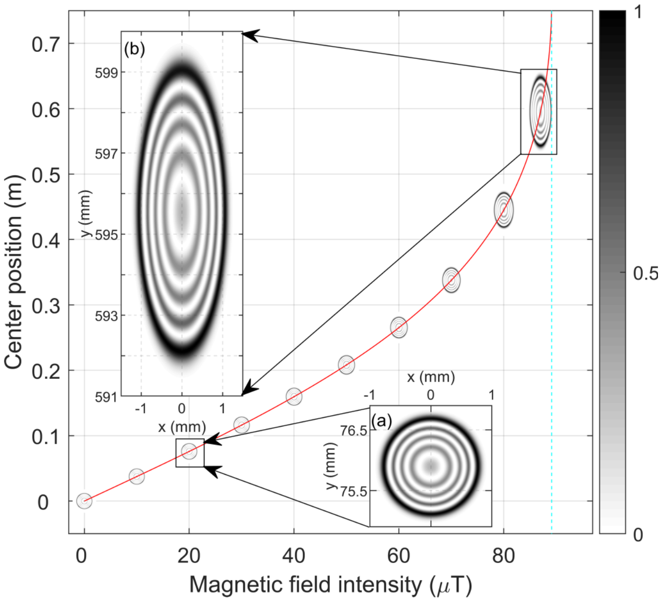

FIG. 7. Calculated center of the interference pattern obtained in photodetachment microscopy along the $\mathbf{E} \times \mathbf{B}$ direction as a function of the intensity of the magnetic field (solid red line). The interference pattern corresponds to an isotropic emission (electron s wave). The vertical blue line determines the maximum value allowed for the $\mathbf{B}$-field intensity. Amplified ($\times 15$) interference patterns for different intensities of the magnetic field are shown along the line. Detailed interferograms are shown in insets (a) and (b) for magnetic-field intensities of 20 μT and 87 μT, respectively.

VII. DISCUSSION AND CONCLUSIONS

In summary, we have presented a detailed theoretical description of the near-threshold photodetachment microscopy when a transverse magnetic field is superimposed to the standard electric field. Since the exact quantum solution is not accessible in a closed form, we have consistently used two different approaches to determine the outgoing electron wave function, namely the quantum source theory with the energy-Green function evaluated by means of the stationary phase approximation and the closed-orbit theory. We have discussed the theoretical derivations for each method and compared their results. In these experiments, the energy of the particles is often controlled, while the time of travel is not; and under these circumstances the energy-dependent Green function is relevant for the description of the system. Although the quantum source formalism provides an excellent basis for the theoretical analysis of the electron propagation in the region with external fields, in this particular case, the commonly used approximation to calculate wave functions associated to regular trajectories, the closed-orbit theory, yields faster numerical results.

Both approaches rely on the study of the classical motion and the family of classical trajectories from the source to the detection plane. In this regard, we have found that within the sector of classically allowed motion all the possible arrival points at the detector are reached by two trajectories, as in the standard case of only the electric field accelerating the photodetached electron. In consequence, we extended for this field's configuration the argument that the interference pattern observed can be explained by the interference between the two classical paths [5,9,13,37,49]. Moreover, we have described the surface enveloping all the allowed classical trajectories—the caustic surface. In this configuration, the caustic surface is not as simple as the paraboloid obtained when only the electric field is present. Indeed, a function of the surface cannot be explicitly obtained, but from the numerical analysis of the classical trajectories we have observed and qualitatively described the effects of the magnetic field on the envelope: a global drift due to the shift of the trajectories [7,19]. Consequently, we have studied the boundary between the classically allowed and classically forbidden zones at the detector, which confines the recorded electron flux distribution in photodetachment microscopy.

In the crossed fields configuration, two different effects on the recorded spatial electron distribution have been studied in detail: (i) the global shift of the pattern along the $\mathbf{E}\times\mathbf{B}$ direction and (ii) the changes of the shape of the interference pattern when the intensity of the magnetic field is increased. For the first one, the Lorentz force produces a global drift of all the classical trajectories of the electron along the $\mathbf{E}\times\mathbf{B}$ direction, such that the measured spatial electron distribution is displaced with respect to the no **B**-field case. We have successfully obtained theoretical expressions to quantify the displacement of the recorded pattern, showing that it becomes larger as the intensity of the transverse magnetic field increases. This matches early experimental and theoretical demonstrations [7]. Regarding the shape of the interference pattern, we focused on the characterization of the classically allowed region and its border, since it confines the electron spatial distribution. The commonly claimed circular pattern turns over an elliptic shape while the magnetic field becomes stronger. We have fully described the ellipse and its eccentricity as a function of the quantities controlled in the experiment. Pursuing this observation, we notice that the variation on the eccentricity is produced as a consequence of a quick elongation of the length of the pattern along the y axis and its slower variation along the x axis in the presence of the transverse magnetic field.

The dependence of the recorded electron distribution on the angular momentum has been investigated for s waves and p waves. The features concerning the pattern position and its shape, within the descriptions here developed, are rooted in classical dynamics and are independent of the nature of the negative ion and the electron angular distribution. However, the ring distribution does depend on the orbital angular momentum and magnetic number of the emitted electron, as depicted in Fig. 6. It is worth noticing that the equation

$$N_{\text{rings}} \cong \frac{2}{3\pi}\frac{\mathcal{E}}{\hbar\gamma}\sqrt{\frac{2\mathcal{E}}{m}}, \tag{65}$$

which estimates the number of rings for the case with only static electric field [6], still holds for the case with a transverse magnetic field. Similarly, the intensity of the electric field in order to observe interference patterns must be such that

$$E < \frac{\sqrt{2m}}{3\pi\hbar q}\mathcal{E}^{3/2}, \tag{66}$$

and together with a set of other inequalities provided the resolution of the experimental apparatuses, as reported [6]. Hence, in order to fully determine the conditions and set the proper orders of magnitude for the observation of the characteristic interference pattern in photodetachment microscopy with crossed electric and magnetic fields, we remarked that the transverse magnetic field must satisfy Eq. (31), which fixes an upper limit for its allowed intensity. As a result, the displacement of the pattern is limited, as well as the eccentricity ($e < 1$).

The results, in either approach, are in agreement with the findings in reported photodetachment experiments [7,19,22], and they offer a clear prediction about the physical phenomena to be observed for the whole range of allowed intensities of the transverse magnetic field. Furthermore, this problem serves to illustrate the power of both semiclassical methods and their correspondence. We hope this contribution encourages further experiments on these topics.

ACKNOWLEDGMENTS

This work was supported by the National Natural Science Foundation of China (NSFC), Grants No. 11474079 and No. 11421063. K.T. acknowledges financial support from CAS President's International Fellowship Initiative Grant No. 2019PM0109 and also expresses his gratitude to M. Catalano for many stimulating discussions at the earliest stage of this work.

APPENDIX: CALCULATION OF DERIVATIVES FOR THE CONSTRUCTION OF THE MULTIPOLE ENERGY-GREEN FUNCTIONS

In this Appendix, we present the derivatives with respect to the coordinates of the initial position $r_0 = \{x_0, y_0, z_0\}$ needed to explicitly write Eq. (51) in terms of the experimental parameters.

First, we have faced the terms

$$\frac{\partial\mathcal{W}_j}{\partial r_0} = \left.\frac{\partial\mathcal{S}(\mathbf{r}_f,\mathbf{r}_0;T)}{\partial r_0}\right|_{T_j}, \tag{A1}$$

where j may take the values 1 and 2, in reference to the two classical trajectories with times of flight T_1 and T_2. Thus, given the classical action, Eq. (9), we get

$$\frac{\partial \mathcal{W}_j}{\partial x_0} = -\frac{m(x_f - x_0)}{T_j},$$
$$\frac{\partial \mathcal{W}_j}{\partial y_0} = -\frac{m\omega}{2}\left(z_D - \frac{2\gamma}{\omega^2}\right) - \frac{m\omega}{2}\cot(\omega T_j/2)\left(y_f - y_0 + \frac{\gamma T_j}{\omega}\right),$$
$$\frac{\partial \mathcal{W}_j}{\partial z_0} = \frac{m\omega}{2}\left(y_f + \frac{\gamma T_j}{\omega}\right) - \frac{m\omega}{2}\cot(\omega T_j/2)(z_D - z_0). \tag{A2}$$

The following terms also appear,

$$\frac{\partial \mathcal{O}_\pm}{\partial r_0} = \frac{\partial \xi_1}{\partial r_0} \pm \frac{\partial \xi_2}{\partial r_0}, \tag{A3}$$

where we have introduced the function ξ_j with $j = 1, 2$ as

$$\xi_j = \left((-1)^{1+j} T_j \sin^2(\omega T_j/2) \left.\frac{\partial^2 \mathcal{S}}{\partial T^2}\right|_{T_j}\right)^{-1/2}. \tag{A4}$$

In this way, we focus on the differentiation of ξ_j with respect to the source coordinates. Then

$$\frac{\partial \xi_j}{\partial r_0} = -\frac{(-1)^{j+1}}{2}\xi_j^3 \left\{ T_j \sin^2(\omega T_j/2) \frac{\partial}{\partial r_0}\left(\frac{\partial^2 \mathcal{S}}{\partial T^2}\right)\right|_{T_j} + \left[T_j \sin^2(\omega T_j/2) \left.\frac{\partial^3 \mathcal{S}}{\partial T^3}\right|_{T_j} \left(\left.\frac{\partial^2 \mathcal{S}}{\partial T^2}\right|_{T_j}\right)^{-1} + \sin^2(\omega T_j/2) + \frac{\omega T_j}{2}\sin(\omega T_j)\right] \left.\frac{\partial \mathcal{E}}{\partial r_0}\right|_{T_j} \Bigg\}. \tag{A5}$$

Here, the energy $\mathcal{E}$ refers to Eq. (13) and their derivatives cast

$$\frac{\partial \mathcal{E}}{\partial x_0} = -\frac{m(x_f - x_0)}{T^2}, \tag{A6a}$$

$$\frac{\partial \mathcal{E}}{\partial y_0} = -\frac{m\omega^2}{4}\csc^2(\omega T/2) \times \left(y_f - y_0 - \frac{\gamma}{\omega^2}[\sin(\omega T) - \omega T]\right), \tag{A6b}$$

$$\frac{\partial \mathcal{E}}{\partial z_0} = -\frac{m\omega^2}{4}\csc^2(\omega T/2)\left(z_D - z_0 - \frac{2\gamma}{\omega^2}\sin^2(\omega T/2)\right) - m\gamma. \tag{A6c}$$

On the other hand, considering Eq. (15), we compute

$$\frac{\partial^3 \mathcal{S}}{\partial T^3} = -\frac{3m}{T^4}(x_f - x_0)^2 - \frac{m\omega^4}{16}[2 + \cos(\omega T)]\csc^4(\omega T/2) \times \left[\left(y_f - y_0 + \frac{\gamma T}{\omega}\right)^2 + (z_D - z_0)^2\right] + \frac{3m\gamma}{4}\csc^2(\omega T/2)\cot(\omega T/2) \times [\omega^2(y_f - y_0) + \gamma\omega T - \gamma\tan(\omega T/2)]$$

and

$$\frac{\partial}{\partial x_0}\left(\frac{\partial^2 \mathcal{S}}{\partial T^2}\right) = -\frac{2m(x_f - x_0)}{T^3}, \tag{A7a}$$

$$\frac{\partial}{\partial y_0}\left(\frac{\partial^2 \mathcal{S}}{\partial T^2}\right) = -\frac{m\omega^3}{4}\cot(\omega T/2)\csc^2(\omega T/2) \times \left(y_f - y_0 - \frac{\gamma}{\omega^2}[2\tan(\omega T/2) - \omega T]\right), \tag{A7b}$$

$$\frac{\partial}{\partial z_0}\left(\frac{\partial^2 \mathcal{S}}{\partial T^2}\right) = -\frac{m\omega^3}{4}\cot(\omega T/2)\csc^2(\omega T/2)(z_D - z_0). \tag{A7c}$$

Given all the above equations, the energy-Green functions Eqs. (40)–(42) are fully determined via Eq. (46) and Eq. (50); consequently, the construction of the multipole electron wave functions go straightforwardly. The explicit expressions in terms of T_1, T_2, $\mathbf{r}_f$, $\mathbf{r}_0$, ω, and γ are rather long and complicated in the writing, and do not contribute to the understanding of the phenomena; therefore, they are not shown here.

[1] G. Mollenstedt and H. Duker, Z. Phys. **145**, 377 (1956).
[2] G. F. Missiroli, G. Pozzi, and U. Valdre, J. Phys. E **14**, 649 (1981).
[3] J. Baudon, R. Mathevet, and J. Robert, J. Phys. B **32**, R173 (1999).
[4] F. Hasselbach, Rep. Prog. Phys. **73**, 016101 (2009).
[5] C. Blondel, C. Delsart, and F. Dulieu, Phys. Rev. Lett. **77**, 3755 (1996).
[6] C. Blondel, C. Delsart, F. Dulieu, and C. Valli, Eur. Phys. J. D **5**, 207 (1999).
[7] W. Chaibi, C. Blondel, C. Delsart, and C. Drag, Europhys. Lett. **82**, 20005 (2008).
[8] I. I. Fabrikant, Zh. Eksp. Teor. Fiz. **79**, 2070 (1980) [Sov. Phys. JETP **52**, 1045 (1980)].
[9] Y. N. Demkov, V. D. Kondratovich, and V. N. Ostrovskii, Pis'ma Zh. Eksp. Teor. Fiz. **34**, 425 (1981) [JETP Lett. **34**, 403 (1981)].
[10] I. I. Fabrikant, Zh. Eksp. Teor. Fiz. **83**, 1675 (1982) [Sov. Phys. JETP **56**, 967 (1982)].
[11] M. L. Du, Phys. Rev. A **40**, 4983 (1989).
[12] I. I. Fabrikant, J. Phys. B **23**, 1139 (1990).
[13] C. Bracher, W. Becker, S. A. Gurvitz, M. Kleber, and M. S. Marinov, Am. J. Phys. **66**, 38 (1998).
[14] C. Blondel, W. Chaibi, C. Delsart, C. Drag, F. Goldfarb, and S. Kröger, Eur. Phys. J. D **33**, 335 (2005).
[15] W. Chaibi, C. Delsart, C. Drag, and C. Blondel, J. Mol. Spectrosc. **239**, 11 (2006).
[16] C. Bracher and A. Gonzalez, Phys. Rev. A **86**, 022715 (2012).

[17] C. Bracher, T. Kramer, and J. B. Delos, Phys. Rev. A **73**, 062114 (2006).

[18] C. Bracher and J. B. Delos, Phys. Rev. Lett. **96**, 100404 (2006).

[19] W. Chaibi, R. J. Peláez, C. Blondel, C. Drag, and C. Delsart, Eur. Phys. J. D **58**, 29 (2010).

[20] T. Kramer, C. Bracher, and M. Kleber, J. Opt. B: Quantum Semiclass. Opt. **6**, 21 (2004).

[21] T. Kramer and C. Bracher, in *Symmetries in Science XI*, edited by B. J. Gruber, G. Marmo, and N. Yoshinaga (Kluwer Academic Publishers, Dordrecht, 2005), pp. 317–353.

[22] X. J. Chen, K. Titimbo, and M. L. Du, Europhys. Lett. **123**, 30008 (2018).

[23] M. L. Du and J. B. Delos, Phys. Rev. A **38**, 5609 (1988).

[24] N. D. Gibson, B. J. Davies, and D. J. Larson, Phys. Rev. A **47**, 1946 (1993).

[25] N. D. Gibson, B. J. Davies, and D. J. Larson, Phys. Rev. A **48**, 310 (1993).

[26] N. D. Gibson, M. D. Gasda, K. A. Moore, D. A. Zawistowski, and C. W. Walter, Phys. Rev. A **64**, 061403(R) (2001).

[27] V. P. Maslov and M. V. Fedoriuk, *Semi-Classical Approximation in Quantum Mechanics*, Mathematical Physics and Applied Mathematics Vol. 7 (Reidel, Dordrecht, 1981).

[28] I. I. Fabrikant, Phys. Rev. A **43**, 258 (1991).

[29] A. D. Peters and J. B. Delos, Phys. Rev. A **47**, 3020 (1993).

[30] R. P. Feynman and A. R. Hibbs, *Quantum Mechanics and Path Integrals*, International Series in Pure and Applied Physics (McGraw-Hill, New York, 1965).

[31] J. B. Delos, in *Advances in Chemical Physics*, edited by I. Prigogine and S. A. Rice (John Wiley & Sons, Inc., Hoboken, NJ, 1986), Vol. 65, pp. 161–214.

[32] M. C. Gutzwiller, *Chaos in Classical and Quantum Mechanics* (Springer, New York, 1990).

[33] L. Schulman, *Techniques and Applications of Path Integration* (Dover Publications, Inc., New York, 2005).

[34] M. Child, *Semiclassical Mechanics with Molecular Applications*, 2nd ed. (Oxford University Press, Oxford, UK, 2014).

[35] T. Kramer, C. Bracher, and M. Kleber, J. Phys. A **35**, 8361 (2002).

[36] W. Becker and M. Kleber, Phys. Scr. **94**, 023001 (2019).

[37] C. Bracher, T. Kramer, and M. Kleber, Phys. Rev. A **67**, 043601 (2003).

[38] E. G. P. Rowe, J. Math. Phys. **19**, 1962 (1978).

[39] E. J. Weniger, Collect. Czech. Chem. Commun. **70**, 1225 (2005).

[40] E. J. Weniger and E. O. Steinborn, J. Math. Phys. **24**, 2553 (1983).

[41] C. F. de Souza and A. de Souza Dutra, Am. J. Phys. **57**, 330 (1989).

[42] L. M. Nieto, J. Math. Phys. **33**, 3402 (1992).

[43] *Handbook of Mathematical Functions: With Formulas, Graphs, and Mathematical Tables*, edited by M. Abramowitz and I. A. Stegun, Dover Books on Mathematics, 9th ed. (Dover Publications, New York, 2013).

[44] M. L. Du and J. B. Delos, Phys. Rev. A **38**, 1913 (1988).

[45] M. L. Du and J. B. Delos, Phys. Rev. A **38**, 1896 (1988).

[46] M. L. Du, Phys. Rev. A **70**, 055402 (2004).

[47] B. C. Yang, J. B. Delos, and M. L. Du, Phys. Rev. A **89**, 013417 (2014).

[48] M. Deng, W. Gao, R. Lu, J. B. Delos, L. You, and H. P. Liu, Phys. Rev. A **93**, 063411 (2016).

[49] M. L. Du, Phys. Rev. A **40**, 1330 (1989).